
# Improved efficiency with concave cavities on S3 surface of a rim-driven thruster

Physics of Fluids ARTICLE pubs.aip.org/aip/pof

# Improved efficiency with concave cavities on $S_3$ surface of a rim-driven thruster

Cite as: Phys. Fluids **35**, 107102 (2023); doi: 10.1063/5.0168698
Submitted: 20 July 2023 · Accepted: 11 September 2023 ·
Published Online: 3 October 2023



Peng Li (李鹏),[1] Hua-Dong Yao (姚华栋),[2] Chao Wang (王超),[1,a)] and Kaiqiang Weng (翁凯强)[1]

## AFFILIATIONS

[1]College of Shipbuilding Engineering, Harbin Engineering University, Harbin 150001, People's Republic of China
[2]Department of Mechanics and Maritime Sciences, Chalmers University of Technology, Gothenburg 41296, Sweden

[a)]Author to whom correspondence should be addressed: wangchao0104@hrbeu.edu.cn

## ABSTRACT

Rim-driven thrusters (RDT) are of great interest for the development of integrated electric motors for underwater vehicles. Gap flow is one of the most prominent flow characteristics and plays an important role in the hydrodynamic performance of RDT. In this study, the rim in a carefully designed RDT was modified with several concave cavities defined by four parameters, and their influence on hydrodynamics was carefully calculated and analyzed. The simulations were performed using the $k$-$\omega$ shear stress transport turbulence model by solving the unsteady Reynolds-averaged Navier–Stokes equations. The numerical method was verified using a popular combination. The numerical results showed that the concave cavities on the rim improve the propulsive efficiency of RDT by a maximum of 3.52%. The increase in the propulsive efficiency is directly associated with the parameters of the concave cavities. Nevertheless, the flow in the gap has a negligible effect on the main flow field through the RDT. According to the numerical analysis, the different pressure integrals at the front and back surfaces of the concave cavities are the main reason for the improvement of the propulsive efficiency. The modification of the rim is helpful and practical for the hydrodynamic optimization of the RDT.



## I. INTRODUCTION

With the development of integrated electric motors, rim-driven thrusters (RDTs) have become an innovative propulsion device for naval vessels.[1] The electric motor stator, which is integrated into the duct, drives a magnetic ring around the blade. RDTs have many advantages owing to their unique design without penetrating shafting. Therefore, the study of RDT is important for the technological advancement of marine vehicles and will be a popular subject in the foreseeable future.[2]

The earliest original geometry of RDT was proposed in a novel patent approximately 80 years ago.[3] Compared to shafting-driven propellers, the ingenious design outperforms the RDT as follows:[4] (i) The compact arrangement saves cabin rooms and is helpful for flexible installation. (ii) The higher motor efficiency is due to the broadband torque transmission through the magnetic field. (iii) The RDT has higher efficiency and is much less sensitive to advance coefficients than a hub-driven propeller. (iv) Low demand for secondary systems: The inherent integration makes this thruster independent of the cooling system and other systems. These advantages have attracted considerable attention in the research community. Research on the RDT performance and application has made significant progress in recent years with the development of integrated motor technologies. Electric motors are currently the most important research topic. Researchers have focused their efforts on improving the electromagnetic performance, sealing, and weight. Another interesting topic is the optimization of bearings used in RDTs. Water-lubricated bearings are a typical, simple, and environmentally friendly choice for commercial company products.[5]

So far, some work has been done on the hydrodynamic performance, which we focus on here. There are little public data on RDT to support academic studies. Therefore, derivatives of ducted propellers,[6] combinations of Ka4–70 and MARIN 19A, and Ka4–70 and MARIN 37 have often been used. Despite the geometric differences between the modified ducted propeller and RDT, adequate experimental and numerical data available in the public literature can help researchers understand their results. In addition, few institutions have designed and manufactured a prototype RDT[7,8] that had been tested in-house, and the data have limited access. Potential flow methods, for example, the lifting surface and boundary element methods, are frequently used for design and selection. The efficiency of these methods was much higher than that of the computational fluid dynamics (CFD) method. Nevertheless, CFD remains the most widely used and economical

method for scholars and engineers to overcome the challenges in applying RDT. In the current study, unsteady Reynolds-averaged Navier–Stokes (URANS) accounted for a large proportion of patients. The $k$-$\omega$ shear stress transport (SST) is one of the main turbulence models that we are aware of.[6,9] The cost and difficulty of this method are lower than DES (detached eddy simulation) and LES (large eddy simulation) according to Refs. 10 and 11. Most of the experiments that considered RDT were classified. Therefore, limited test data can be found in the literature by the public.[12]

Based on the above geometries and common methods, researchers have conducted some studies on the hydrodynamics and optimization of RDT. Song *et al.*[13] conducted simulations of the hydrodynamics of four pairs of RDTs with and without hubs. They pointed out that the presence of a hub reduces the hydrodynamic efficiency by up to 2%. There are three reasons for this loss. (i) Lower flow rate pushes the fluid through the hub-type RDT faster, which reduces the angle of attack along the radial blade. (ii) Higher flow rate and viscosity of the fluid increase the flow velocity; (iii) more vorticity induced by the hub leads to more energy loss. Zhu and Liu[14] conducted tests and determined a head curve for a seven-bladed RDT pump. They found that the curve had a hump shape and pointed out three causes for the hump shape: the backflows residing near the gap, the difference between the pressure side and the suction side, and the pressure loss within a half radius. They then analyzed the influence of the hub on the efficiency of the RDT and reached the same conclusion as in Ref. 13. Lü *et al.*[15] discussed the performance of a distributed pump-jet propulsion system attached to a submarine by solving the RANS equations. Researchers from Wuhan University of Technology have extensively studied the hydrodynamic performance of RDT.[13] They pointed out that the gap between the duct and rim has a significant influence on the hydrodynamics of the rim-driven contra-rotating thruster (RDCRT) and believed that the frictional torque acting on the gap is strictly related to the clearance size, rotation rate, and advance coefficients. In addition, they proposed that a proper fillet at the corner of the gap could reduce the torque loss, and their numerical and experimental data on torque loss agreed well. Lin *et al.*[4] used the OpenFOAM solver to determine how the shape of the gap affects the hydrodynamics of RDT and concluded that the efficiency could be improved by shortening the gap length. $y+$ over the S surfaces has an impact on the distribution of the tangential velocity in the gap. Then, they proposed a modified formula to calculate the frictional torque between the S surfaces. They evaluated four different thrusters and assessed their hydrodynamic properties. They selected the best one to perform the tests, and the numerical and experimental results agreed well. Grümmer *et al.*[8] applied a class-and-shape transformation (CST) method to create multiple ducts, and the blade was adjusted based on a good design. The speed of the vehicle increases from 1.22 to 1.46 m/s for the same power.

From the above reviews, it can be seen that researchers made efforts to improve the propulsive efficiency by optimizing the duct profile or the shape of the gap. However, the results have been unsatisfactory. This study focuses on the optimization of the rim, which can change the characteristics and magnitudes of the torque acting on the $S_3$ surface. This will significantly improve the propulsive efficiency of the RDT. The study was conducted using numerical simulations in which the URANS equations were solved. The paper is organized as follows: The governing equations, geometries, computational domain, boundary conditions, and grids are presented in Sec. II. The hydrodynamic results, flow characteristics, and optimization mechanism are presented and discussed in Sec. III. In Sec. IV, we present several conclusions based on our data and preview prospects for future studies.

## II. NUMERICAL DETAILS

### A. Governing equations and turbulence model

The URANS equations can be written as follows:

$$\frac{\partial \rho}{\partial t} + \nabla \cdot (\rho \bar{\mathbf{v}}) = 0, \tag{1}$$

$$\frac{\partial}{\partial t}(\rho \bar{\mathbf{v}}) + \nabla \cdot (\rho \bar{\mathbf{v}} \otimes \bar{\mathbf{v}}) = -\nabla \cdot \bar{p}\mathbf{I} + \nabla \cdot (\bar{\mathbf{T}} + \mathbf{T}_{\mathrm{RANS}}) + \mathbf{f}_b, \tag{2}$$

where $\bar{\mathbf{v}}$ is the mean velocity, $\bar{p}$ is the mean pressure, $\rho$ is the fluid density, $\mathbf{I}$ is the identity tensor, $\bar{\mathbf{T}}$ is the mean viscous stress tensor, and $\mathbf{f}_b$ is the result of the body forces (such as gravity and centrifugal forces). The $k$-$\omega$ SST turbulence model is a two-equation turbulence model that solves the transport equations for the turbulent kinetic energy (TKE) $k$ and the specific rate $\omega$ (the dissipation rate per unit turbulent kinetic energy). It is used to ensure the closure equation and has been proven in numerous studies on the hydrodynamic predictions of RDT[16–18] and traditional propellers.[19–22] The transport equations for $k$ and $\omega$ are as follows:

$$\frac{\partial}{\partial t}(\rho k) + \nabla \cdot (\rho k \bar{\mathbf{v}}) = \nabla \cdot \left[(\mu + \sigma_k \mu_t)\nabla k\right] + P_k - \rho \beta^* f_{\beta^*}(\omega k - \omega_0 k_0) + S_k, \tag{3}$$

$$\frac{\partial}{\partial t}(\rho \omega) + \nabla \cdot (\rho \omega \bar{\mathbf{v}}) = \nabla \cdot \left[(\mu + \sigma_\omega \mu_t)\nabla k\right] + P_\omega - \rho \beta f_\beta(\omega^2 - \omega_0^2) + S_\omega, \tag{4}$$

where $\mu$ is the dynamic viscosity; $\sigma_k$ and $\sigma_\omega$ are model coefficients; $P_k$ and $P_\omega$ are production terms; and $f_{\beta^*}$ and $f_\beta$ are the modification factors for free-shear and vortex-stretching, respectively. $S_k$ and $S_\omega$ are the user-specified source terms. Detailed information can be found in Ref. 23.

### B. Geometry and modifications of the rim

The RDT used in this paper is named m1SP974, where m1 means the first version of modification based on a rim developed by the authors previously; 9, 7, and 4 are the number of the pre-stator (PS) blades, the blades, and the post-stator blades, respectively. It was carefully designed and optimized for further numerical and experimental investigations. Its geometry is shown in Fig. 1. As can be seen from the figure, the RDT consists of six assemblies: a fair water duct, one single annular rim, nine streamlined pre-stators (PS), seven blades with moderate skewness, four symmetrical rear-stators (RS), and an elongated hub. The stators are helpful for the structural strength of RDT. In addition, the pre-stator provides the blades flow of higher quality and improves its propulsive efficiency. The geometric parameters are listed in Table I. The coordinate system is located at the rotating center around which the rotor (the combination of rim, blades, and partial hub) rotates. The positive $x$ axis points downstream, whereas the $y$ and $z$ axes are in the plane perpendicular to the $x$ axis.

As shown in Fig. 2, several parameters were used to determine the layout of the concave cavities on the $S_3$ surface of the circular rim.

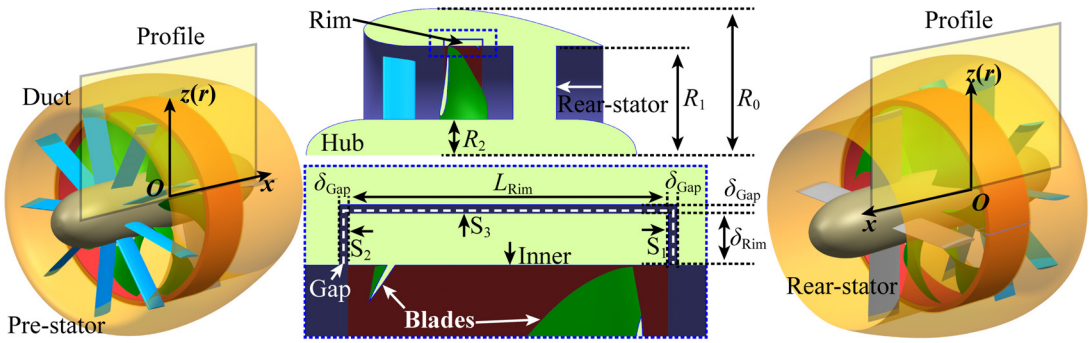


**FIG. 1.** The geometry of the RDT is termed m1SP974.

**TABLE I.** Key parameters of the RDT m1SP974.

| Item | Symbol | Unit | Value |
|---|---|---|---|
| Maximum duct radius | $R_0$ | mm | 142.6 |
| Blade radius/duct inner radius/ rim inner radius | $R_1$ | mm | 105.5 |
| Rim outer radius | $R_2$ | mm | 111.5 |
| $R_2$ minus the thickness of the concave cavity | $R_3$ | Mm | ⋯ |
| Hub ratio | ⋯ | ⋯ | 0.316 |
| Gap thickness | $\delta_{Gap}$ | mm | 1.0 |
| Rim thickness | $\delta_{Rim}$ | mm | 6.0 |
| Duct length | $L_{Duct}$ | mm | 235.1 |
| Rim length | $L_{Rim}$ | mm | 56.0 |
| Blade chord at $0.7R_1$ | $C_{0.7R1}$ | mm | 81.8 |
| Pre-stator chord | $C_{PS}$ | mm | 32.5 |
| Rear-stator chord | $C_{RS}$ | mm | 42.7 |

The width of the concave cavity ($W$) was defined as the axial distance between the two side surfaces, as shown in Fig. 2(c). The thickness ($H$) is the radial distance between the $S_3$ surface and the bottom surface of the concave cavity, as shown in Fig. 2(b). The circumferential span of a single cavity ($\varphi_1$) is easily understood, as shown in Fig. 2(b). The circumferential span between two cavities ($\varphi_2$) is equal to 360° divided by the number of concave cavities that lie on the rim. The detailed parameters of the concave cavity are listed in Table II. $N$ is the number of the concave cavities distributed on the rim. The layouts were classified into four categories based on the above four parameters. When necessary, we use m0–m3 to refer to different cases in a single category. The original case was included in all categories and set as the reference case.

### C. Computational domain, boundary conditions, and meshing

The computational domain is a cylinder with a streamwise length of $38R_1$ and a radius of $12R_1$, as illustrated in Fig. 3(a). Here, $R_1$ is the radius of the inner surface of the duct The size of the computational domain used is sufficient based on previous research.[12,14,16,24,25] The origin of the coordinate system is located at the center of the rotor, as shown in Figs. 1 and 3(a). The velocity inlet lies $14R_1$ upstream, whereas the pressure outlet is located $24R_1$ downstream, far from the origin. The inlet surface is set with the velocity inlet boundary condition, and the outlet surface with the pressure outlet boundary condition. The cylindrical boundary of the computational domain is set as a slip wall. The rotating subdomain is set up to enclose the rotor. Noting the division of the subdomains is the same as that used by Zhai *et al.*,[12] which is believed to be more accurate according to their findings. In our study, STAR-CCM+ is taken as the solver for the numerical simulations. The pressure–velocity coupling is based on the SIMPLEC algorithm. A second-order upwind scheme is used for the convective term.

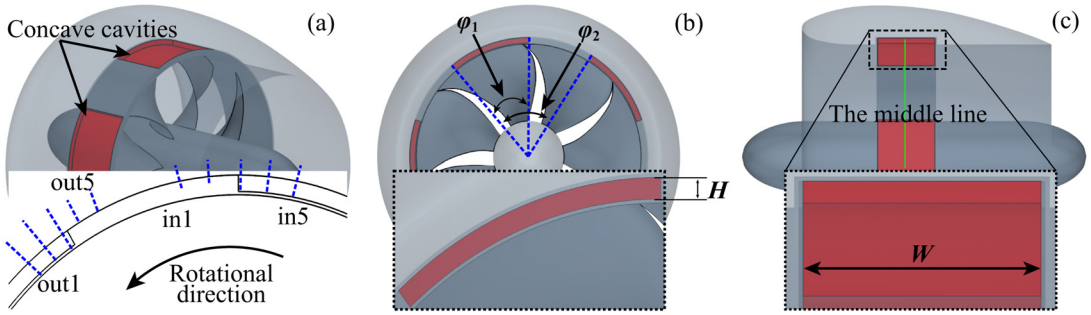


**FIG. 2.** The layout of the concave cavities in the case: M1 which has five cavities.

**TABLE II.** The detailed information about the modification of the rim.

| Case No. | $W$ | $H$ | $\varphi_1$ | $\varphi_2$ | $N$ |
|---|---|---|---|---|---|
| M0 | ... | ... | ... | ... | 0 |
| M1 | 54 | 5 | 40 | 72 | 5 |
| M2 | 34 | 5 | 40 | 72 | 5 |
| M3 | 44 | 5 | 40 | 72 | 5 |
| M4 | 54 | 1 | 40 | 72 | 5 |
| M5 | 54 | 3 | 40 | 72 | 5 |
| M6 | 54 | 5 | 20 | 72 | 5 |
| M7 | 54 | 5 | 30 | 72 | 5 |
| M8 | 54 | 5 | 40 | 120 | 3 |
| M9 | 54 | 5 | 40 | 90 | 4 |

A first-order implicit scheme is used for temporal discretization, and five inner iterations are set for each time step.

Trimmer and prism layer techniques were used to create an unstructured grid to fill the computational space. Six layers of sheet cells with a radial expansion coefficient of 1.2 are attached to the non-slip wall, so that the dimensionless wall distance $y+$ remains within 54. The face and volume of the cells were controlled based on the base value. Detailed information about the distribution of the different cells is listed in Table III. The minimum and maximum values were appropriate for joint assemblies with different cell requirements. By adjusting the baseline values, three sets of grids listed in Table IV were used to perform the convergence analysis. The reference values for the coarse, medium, and fine grids are 1.0, 0.741, and 0.549 m, respectively. Figure 4 presents the details of the fine grid for the M0. The other cases maintain the same grid strategy, which may result in small variations in the number of cells due to the different rims.

### D. Convergence analysis and verification

The related parameters about the hydrodynamics of RDT are written as follows:

$$J = U_{\text{ref}}/(2nR_1), \tag{5}$$

$$C_{T_{\text{RDT}}} = T_{\text{RDT}}/\left(\rho n^2 (2R_1)^4\right), \tag{6}$$

$$C_{Q_{\text{rotor}}} = Q_{\text{rotor}}/\left(\rho n^2 (2R_1)^5\right), \tag{7}$$

**TABLE III.** Detailed information about the cell sizes of the mesh, which are presented in percentage based on the reference length of reference values.

| Item | Maximum size (%) | Minimum size (%) | Average size (%) |
|---|---|---|---|
| Duct | 0.1 | 0.025 | 0.082 |
| Blades | 0.1 | 0.025 | 0.065 |
| Rim | 0.025 | 0.025 | 0.025 |
| Pre-stator | 0.1 | 0.05 | 0.097 |
| Rear-stator | 0.1 | 0.05 | 0.097 |
| Hub | 0.4 | 0.1 | 0.375 |
| Blade region | ... | ... | 0.1 |
| Inner flow region | ... | ... | 0.2 |
| Duct region | ... | ... | 0.4 |
| Wake region | ... | ... | 0.4 |
| Far wake region | ... | ... | 0.8 |

**TABLE IV.** The cell amount of three grids.

| Item | Coarse | Medium | Fine |
|---|---|---|---|
| Cells in rotor surfaces | 292 888 | 565 478 | 1 080 321 |
| Cells in stator surfaces | 385 270 | 698 637 | 1 214 334 |
| Total number of cells | 13 632 515 | 22 854 632 | 31 874 595 |

$$\eta = JC_{T_{\text{RDT}}}/(2\pi C_{Q_{\text{rotor}}}), \tag{8}$$

where $J$ is the advance coefficient, $U_{\text{ref}}$ is the free-stream velocity, $n$ is the rotational rate of the rotor, $T_{\text{RDT}}$, and $Q_{\text{rotor}}$ are the total thrust of the RDT and the torque acting on the rotor, respectively. The convergence analysis was performed under $J = 0.9$ and $n = 15.6$ rps for M0, as mentioned in Subsection II B. The coefficients of the total thrust and torque acting on the rotor were used to assess the accuracy of the discretization. To perform the convergence analysis, a procedure called grid convergence index (GCI) based on the Richardson extrapolation method[26,27] has been evaluated by numerous CFD simulations.[28–32] Detailed information on this procedure can be found in Celik *et al.*[33] The results of the assessments are listed in Table V. The data in Table V show that the numerical uncertainties based on the fine-grid

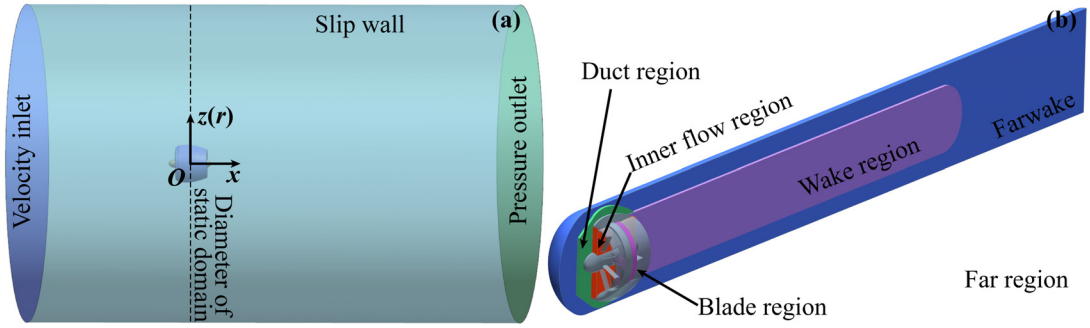


**FIG. 3.** (a) The computational domain and boundary conditions. (b) The division of the computation domain into multiple regions for mesh generation.

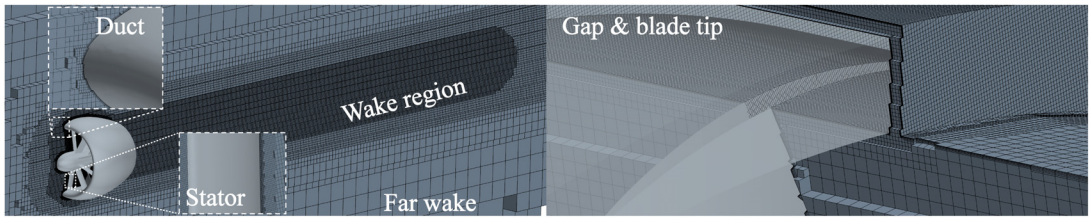


**FIG. 4.** Grid distribution near the RDT and cells in the gap.

**TABLE V.** The results of the convergence analysis.

| Item | For the total thrust coefficient | For the torque acting on the rotor |
|---|---|---|
| $N$ | 13 632 515, 22 854 632, 31 874 595 | 13 632 515, 22 854 632, 31 874 595 |
| $r$ | 1.676, 1.395 | 1.676, 1.395 |
| ϕ | 0.1342, 0.1375, 0.1387 | 0.0810, 0.0846, 0.0859 |
| $p$ | 2.197 | 2.220 |
| $U$ | 1.00% | 1.73% |

solution should be reported as 1.00% and 1.73% for the total thrust and torque acting on the rotor, respectively, implying that our simulations are reliable. Therefore, a fine grid was used for the following calculations. The time step used in our simulations corresponded to the interval at which the blades were rotated by 2°.

Experimental data on RDT are lacking, and the hydrodynamic performance of a popular geometry, a combination of Ka 4–70 and MARIN 19A, was used to validate the numerical results. In addition, experimental data for a ducted propeller by Baltazar *et al.*[34] were used for comparison. The gap thickness in the modified RDT used in this study was the same as in previous studies. The grid is shown in Fig. 5. Note that the rim is disregarded from the comparison as the ducted propeller does. From Fig. 6, it can be seen that good consistency is achieved, which confirms our numerical code and method. Nothing that $C_T$ and $C_Q$ are lightly different from Eqs. (6)–(8). They are defined as $T/(\rho n^2 D^4)$, $Q/(\rho n^2 D^5)$, where $T$ and $Q$ are the thrust and torque acting on the blades, and $D$ is the diameter of the blades. However, an overestimation of the torque coefficient by up to 8.7% resulted in a significant deviation of the propulsive efficiency by up to 16.5%. We believe this is closely related to the friction loss between the duct and the rim, as reported by other researchers.[4] Moreover, large discrepancies have been reported by Lin *et al.*[4] and Liu and Vanierschot.[6] Therefore, we believe that the simulation results are reliable.

## III. RESULTS AND DISCUSSION

### A. The hydrodynamic results

In this section, the hydrodynamics of the different cases mentioned in Subsection II B are systematically calculated under $J = 0.9$ (the highest propulsive efficiency point for m1SP974) to determine the influence of the rim with concave cavities on the hydrodynamic performance. All hydrodynamic loads were time-averaged over the last 20 revolutions. The hydrodynamics of the different cases are listed in Table VI, where $\Delta\eta$ is the increment in the propulsive efficiency relative to the original case, M0. It can be seen that the concave cavities do have a negligible effect on the total thrust of the RDT. The largest bias between the modified and original cases was less than 0.16%. In addition, the torque acting on the rotor was more susceptible to the

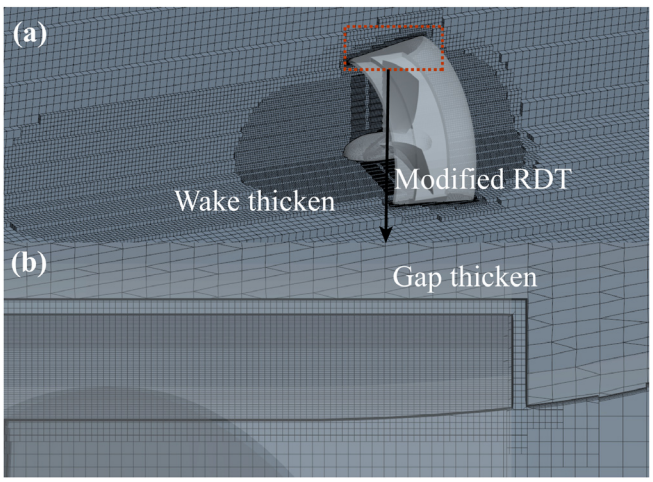


**FIG. 5.** The grid for Ka 4-70 and MARIN 19A.

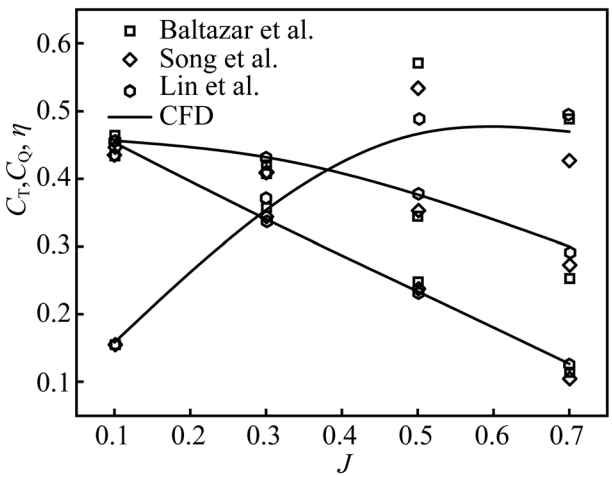


**FIG. 6.** The hydrodynamic performance.

**TABLE VI.** The hydrodynamics of RDT.

| Case No. | $C_{T_{RDT}}$ | $C_{Q_{Rotor}}$ | $\eta$ | $\Delta\eta$ (%) |
|---|---|---|---|---|
| M0 | 0.4320 | 0.1214 | 0.5099 | 0 |
| M1 | 0.4322 | 0.1173 | 0.5279 | 3.52 |
| M2 | 0.4322 | 0.1189 | 0.5208 | 2.14 |
| M3 | 0.4319 | 0.1181 | 0.5238 | 2.72 |
| M4 | 0.4313 | 0.1184 | 0.5217 | 2.32 |
| M5 | 0.4318 | 0.1176 | 0.5250 | 3.11 |
| M6 | 0.4314 | 0.1188 | 0.5202 | 2.01 |
| M7 | 0.4320 | 0.1181 | 0.5239 | 2.75 |
| M8 | 0.4320 | 0.1189 | 0.5203 | 2.04 |
| M9 | 0.4320 | 0.1181 | 0.5238 | 2.73 |

**TABLE VII.** The torque acted on different surfaces of the rim with concave cavities.

| Case No. | $C_{Q_{Inner}}$ | $C_{Q_{S1}}$ | $C_{Q_{S2}}$ | $C_{Q_{S3}}$ |
|---|---|---|---|---|
| M0 | 0.0538 | 0.0057 | 0.0032 | 0.0367 |
| M1 | 0.0583 | 0.0064 | 0.0087 | −0.0138 |
| M2 | 0.0558 | 0.0060 | 0.0057 | 0.0077 |
| M3 | 0.0568 | 0.0061 | 0.0069 | −0.0020 |
| M4 | 0.0563 | 0.0063 | 0.0065 | 0.0042 |
| M5 | 0.0577 | 0.0063 | 0.0079 | −0.0086 |
| M6 | 0.0563 | 0.0060 | 0.0063 | 0.0075 |
| M7 | 0.0576 | 0.0062 | 0.0074 | −0.0039 |
| M8 | 0.0564 | 0.0062 | 0.0061 | 0.0073 |
| M9 | 0.0574 | 0.0063 | 0.0072 | −0.0030 |

modified rims. The reduced torque improved the propulsive efficiency by up to 3.52% for M1.

To gain a deeper insight into the torque acting on the rim, the torques acting on the four surfaces of the rim are presented in Table VII. The partial results from the various cases are also plotted in Fig. 7. For clarity, all cases were classified into four categories according to the parameters of the concave cavity, and each category included four cases with increasing parameters, named m0–m3. Note that the torque acting on each cavity counts in the $S_3$ surface. We can see that the torques acting on $S_2$ and $S_3$ are much smaller than those acting on the inner and $S_3$ surfaces, indicating that the reduced torque depends mainly on these two surfaces. In addition, the torque acting on the inner surface changed compared to the original case (M0) for all modified cases. The bounds of the increments ranged from 3.71% to 8.37%. In contrast, the torque acting on the $S_3$ surface decreased further when a parameter of the concave cavity was increased. Its bounds of decrement ranged from 79.01% to 137.61%, far exceeding the increment in the inner surface. This can be seen in Fig. 7. Two indications can be derived from this: (i) the reduction of the torque on $S_3$ of the rim is the main reason for the increase in the propulsive efficiency, and (ii) the increase in the efficiency is closely related to the reduction of the torque acting on the rim or specifically $S_3$.

The original case and the best optimization case in our study were selected for further comparison. Figure 8 shows the hydrodynamic comparison. It is obvious that the total thrust remains almost constant, whereas the torque acting on the rotor decreases, resulting in improved efficiency, as shown in Fig. 8(a). The first dashed box in Fig. 8(b) shows that the decrease in torque acting on the rim dominates the hydrodynamic variation of the RDT. The second dashed box in Fig. 8(b) shows that the torque acting on $S_3$ is opposite to the torque acting on the rest of the rim, which means that the torque is reduced by 137.7%. Although the torques acting on $S_1$ and $S_2$ increased significantly, their absolute values were at least one order of magnitude smaller than those of $S_3$ and the inner part. Moreover, the torque of the rotor is not significantly affected. Therefore, it was reconfirmed that the reduced torque acting on the $S_3$ surface dominates the variation in the improved propulsive efficiency.

Figure 9 compares the pressure and frictional torque acting on the surfaces of the rims in cases: M0 and M1. It can be seen that in both cases there is no pressure torque acting on the "flat" $S_1$ and $S_2$.

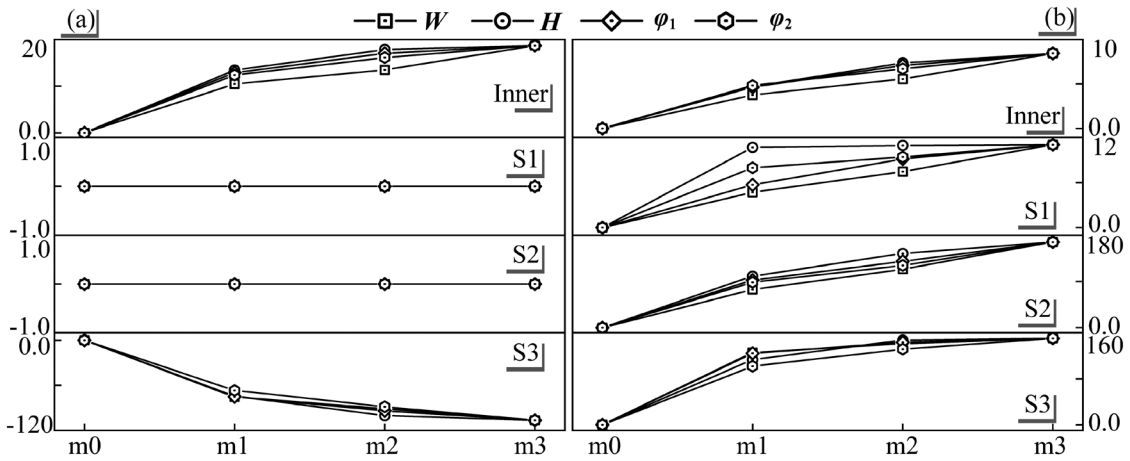


**FIG. 7.** The increment in torque acting on the rim: (a) pressure torque and (b) frictional torque.

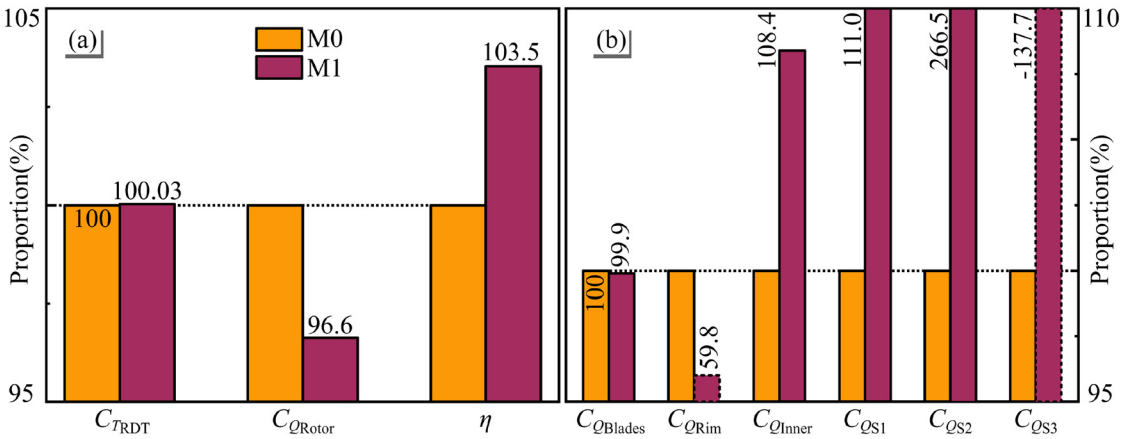


**FIG. 8.** The hydrodynamic comparison between two cases: M0 and M1.

Similarly, no pressure torque is generated from the "flat" $S_3$ for the original case: M0. However, a much larger pressure torque is generated, which is opposite to the frictional torque or torque acting on the rotor, as indicated by the dashed box in Fig. 9(a). At the same time, the frictional torque on each surface increases sharply compared to the original case: M0. Therefore, we can conclude that the reduced torque acting on the $S_3$ surface is attributed to the pressure torque generated by the concave cavities.

### B. The flow through the gap

The flow quantities of the flow field in the following content are the phase-averaged results. The phase-averaged quantity[31] is calculated using the following equation:

$$f(x,y,z) = \frac{1}{A}\sum_{a=1}^{A} f(x,y,z,t_0 + a\Delta t), \tag{9}$$

where $f(x, y, z)$ is the flow quantity under consideration, $A$ is the total number of samples after convergence, $t_0$ is the initial time at which the simulation converges, $a$ is the quantity of the $a$th sample, and $\Delta t$ is the sampling interval. In addition, the phase-averaged quantities can be re-averaged along the tangential direction in a cylindrical coordinate system, as shown in Fig. 1. The re-averaged quantities[30] were time-independent and related only to the spatial resolution in the same simulation.

The flow through the gap is determined by the pressure difference created by the rotating blades. Figure 10 shows the phase-averaged pressure coefficient [$C_p = (p - p_0)/(0.5\rho U_{ref}^2)$, where $p$ and $p_0$ are the local pressure and reference pressure, respectively] and dimensionless tangential velocity ($u_t$) of the flow passing through the gap between M0 and M1. The planes in Fig. 10 were extracted from the gap, as indicated by the dashed lines in Fig. 2(a). The wake ejected from the blades had a much higher pressure than the fluid drawn in by the blades, resulting in a significant pressure difference between $S_1$ and $S_2$. The higher pressure near $S_1$ pushed the fluid in the gap toward $S_2$ where the ambient pressure was lower. Therefore, the flow direction in the radial gap was opposite to the mainstream flow direction in the duct, as illustrated in Fig. 10(a). This was also confirmed by numerous researchers and their studies.[2,4,8,35,36] At the upstream corner, there is a backflow region that can be created by the pressure on $CC_{side1}$ as

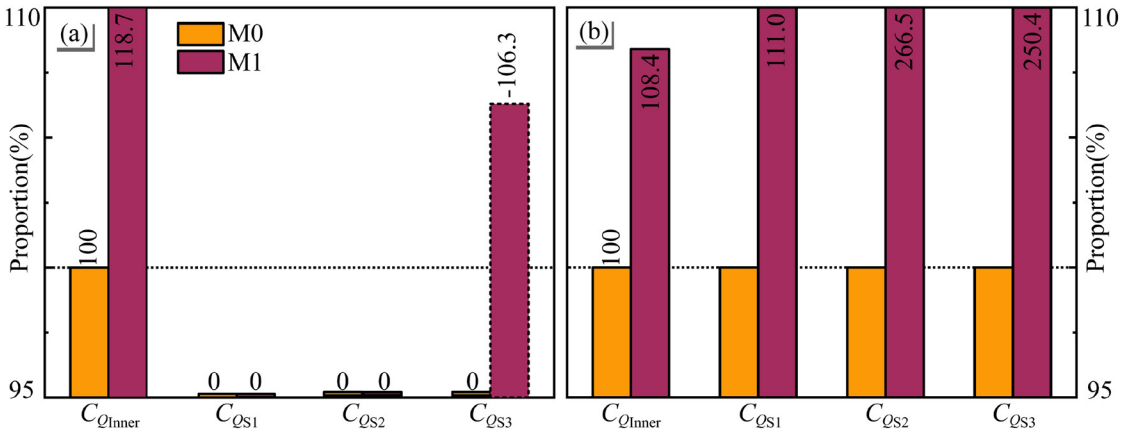


**FIG. 9.** The torque acted on the rim: (a) pressure component and (b) frictional component.

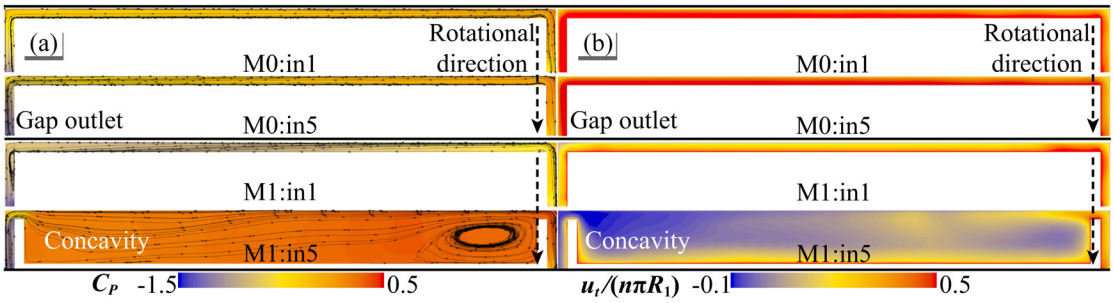


**FIG. 10.** The flow in the gap (a) the axial velocity with constrained streamlines and (b) the tangential velocity in the rotational direction.

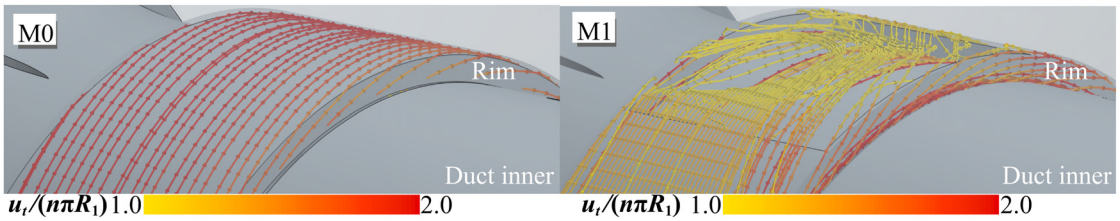


**FIG. 11.** The streamlines through the gap.

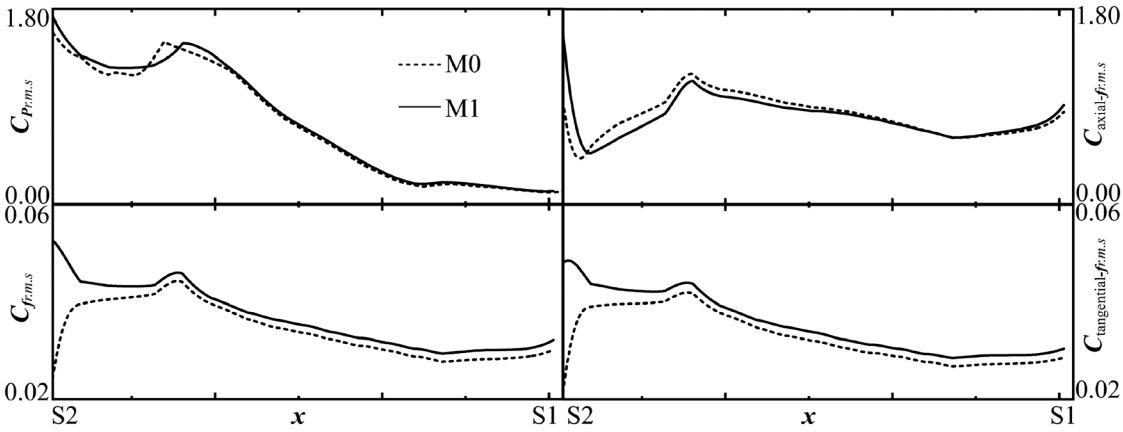


**FIG. 12.** The circumferentially averaged *rms* of the coefficient of pressure and wall shear stress in the inner surface of two rims from two cases: M0 and M1.

marked in Fig. 16. The viscous shear stress induced by the rotating rotor forced the fluid to flow in the rotational direction, as shown in Fig. 10(b). The tangential velocity decreased as the flow moved radially away from the surfaces of the rims M0 and M1. However, the low tangential velocity zone in in5 in Fig. 10(b) suggests that there is a large backflow near the $CC_{side2}$. Figure 11 confirms this inference. Compared to the original M0 case, the fluid moves more slowly and irregularly when it encounters a concave cavity. The fluid slows down due to the backwards-facing step flow.

We believe that the mainstream enclosed by the duct and inhaled by the blades restricts the outflow from the gap close to the inner surface of the rim, which changes the mechanical properties. Figure 12 shows the circumferentially averaged *rms* values of the pressure and wall shear stress acting on the inner surfaces of the rims for cases M0 and M1. As can be seen, the influence of outflow is more pronounced upstream of the leading edge (LE) than downstream of the trailing edge (TE) for the pressure and wall shear stress. Pressure distribution was almost constant the further downstream the flow was. In addition, the wall shear stress immediately downstream of $S_2$ from M1 was significantly altered by the outflow and was slightly stronger than that in the original case. The wall shear stress acting on the inner surface can be divided into axial and tangential components based on the columnar geometry. Apparently, the tangential component dominates the frictional force acting on the inner surface. The axial component behaves similar to the pressure and is enhanced near $S_2$. Figure 13 shows the vortices leakage from the gap with the $Q$ iso-surface colored by turbulent kinetic energy (TKE). $Q$ is defined as follows:

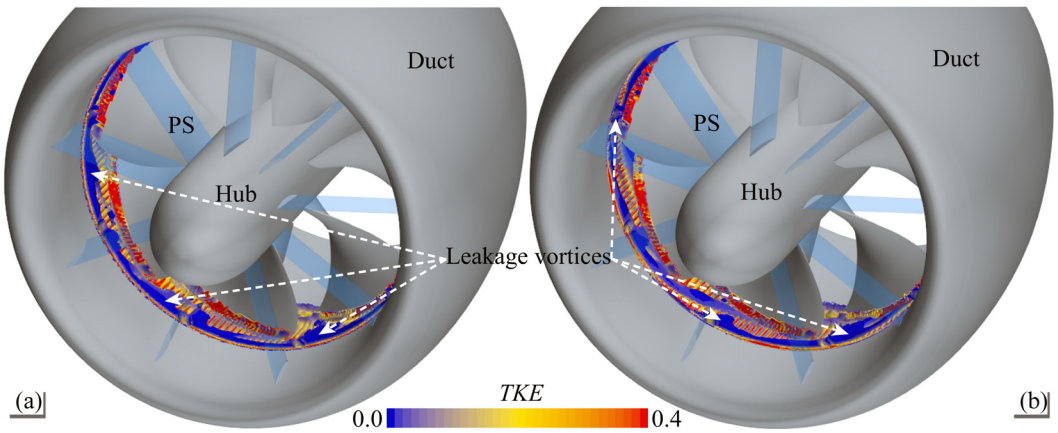


**FIG. 13.** Vortices leakage from the gap outlet for two cases: (a) M0 and (b) M1.

$$Q=\frac{1}{2}\left[\left(\frac{\partial u}{\partial x}\right)^2+\left(\frac{\partial v}{\partial y}\right)^2+\left(\frac{\partial w}{\partial z}\right)^2\right]-\left[\frac{\partial u}{\partial y}\frac{\partial v}{\partial x}+\frac{\partial u}{\partial z}\frac{\partial w}{\partial x}+\frac{\partial v}{\partial z}\frac{\partial w}{\partial y}\right]. \tag{10}$$

As mentioned earlier, leakage vortices with low levels of TKE attach tightly to the inner surface and spread unevenly downstream. The leaky vortices from the two cases shown in Fig. 13 behaved similarly, and limited differences were still observed when they were close to the blade tips. The leakage vortices from the modified case appear to extend farther downstream than in the original case, consistent with the variations shown in Fig. 12.

There is no doubt that restricted leakage vortices would encounter blades at the joints between the blades and rim. The blades prevented the influence of the leakage vortices from extending downstream. Nevertheless, Fig. 14 shows the limited effects of the leakage vortices on the mechanical properties ($C_p$ and $C_f$ are the pressure and friction coefficient) of the blade tip. As shown, the quantities on the pressure side of the blade are more sensitive to the leakage vortices than those on the suction side, which could be related to the thicker boundary layer due to the lower relative velocity between the pressure side and the fluid. In addition, the pressure distribution near the leading edge (LE, and TE means trailing edge) was altered. The optimization reduces the peak pressure, which may be beneficial for reducing the risk of cavitation inception, according to Ref. 37. The wall shear stresses of the two cases varied slightly along the chord and coincided at the trailing edge.

It is believed that the influence of the leakage vortices was blocked by the blades. Nevertheless, we compared the circumferentially averaged *rms* values of the pressure and velocity magnitude in the two types of wakes, as shown in Fig. 15. In general, the effect of optimization on the wake is difficult to observe because the rotational motion of the blades dominates. This finding is consistent with the results reported by Lin *et al.*[4]

### C. The mechanism of the optimization

In the previous analysis, it was believed that the influence of the concave cavity was confined to the gap and front inner surface of the rim. Therefore, concave cavities reduce the torque acting on the rim due to the variations within the gap.

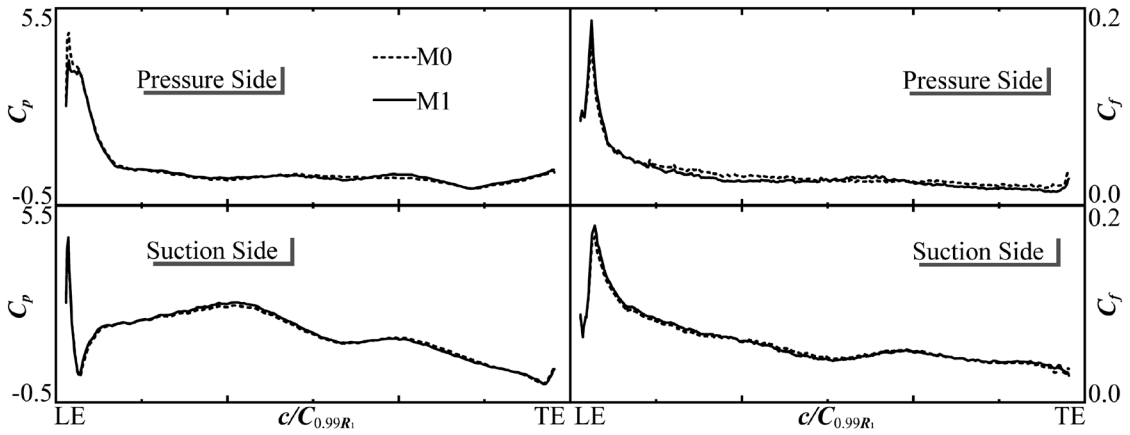


**FIG. 14.** Mean pressure and shear stress on the blades at $r/R_1 = 0.99$ for two cases.

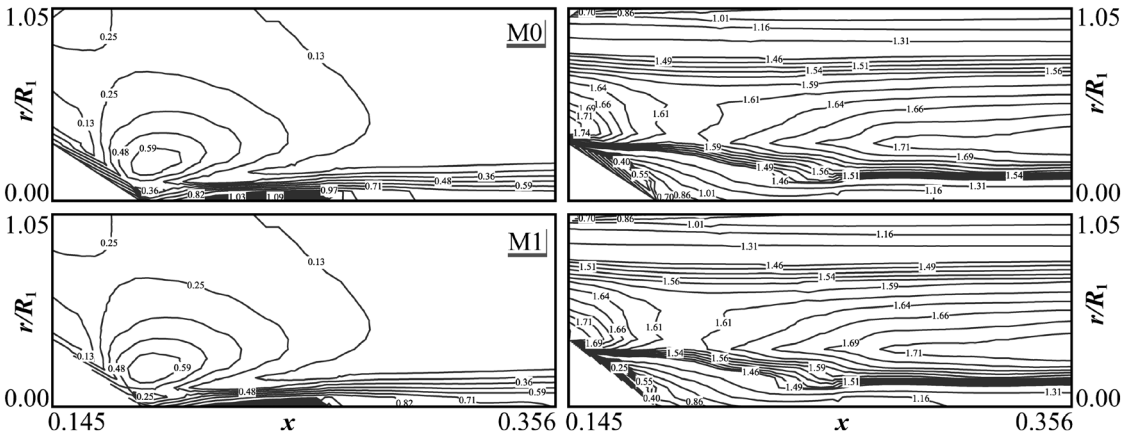


**FIG. 15.** The circumferentially averaged flow quantities in the wake behind the duct [the *rms* of pressure coefficient (left) and dimensionless velocity magnitude (right)].

Figure 16 shows the distributions of the pressure coefficient and dimensionless wall shear stress. The gradients of the mechanical properties on the rim from M0 were smoother and more uniform than those of M1. A strip-shaped high-pressure zone is located at the bottom of $CC_{front}$, whereas a low-pressure zone is located near $CC_{back}$. The distribution of wall shear stress was significantly different. The wall shear stress increased significantly as the flow approached $CC_{in}$ and $CC_{out}$. Except for these regions, the mechanical properties were almost unaffected by the concave cavity. The tangential velocities along the radial lines located at the axial middle of the rim, as shown in Figs. 2(a) and 2(c), were extracted and are plotted in Fig. 17. The tangential velocity is uniformly distributed in a zigzag pattern along the radial direction. In the modified case, the flow in the gap differs significantly and transforms into an L-shape when it falls into a cavity, although it still zigzags in other zones. There was no clear gradient near the outermost gap, indicating that the wall shear stress was low in these zones. In addition, the velocity magnitude was much smaller in the concave cavity zone. To obtain further insight into the characteristics of the tangential velocity, the radial derivative, i.e., the acceleration of the tangential velocity, was calculated and is plotted in Fig. 18. It can be seen that the acceleration is much larger when the fluid approaches or leaves the concave cavity. The $\tau = \mu(du/dn)$ equation shows that the wall shear stress ($\tau$) is proportional to the normal velocity gradient $(du/dn)$. Therefore, a greater acceleration results in an increase in the wall shear stress, as shown in Fig. 16. Although axial velocity contributes to the wall shear stress, the $S_3$ surface data in Tables IX and X imply that the tangential component plays a dominant role in the variation in the wall shear stress.

From Subsection III A, we see that the concave cavities improve the propulsive efficiency of the RDT by reducing the torque acting on

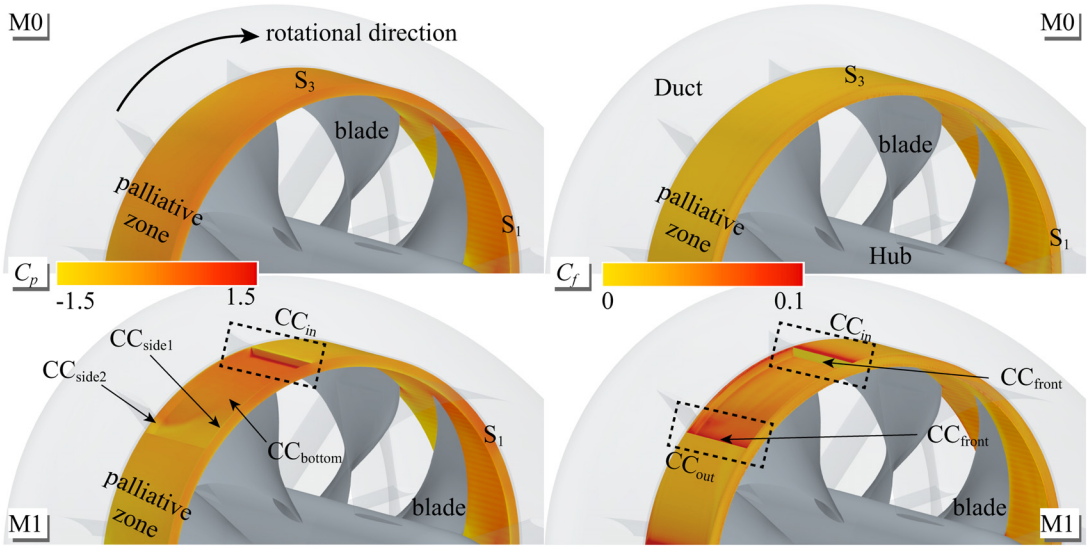


**FIG. 16.** The distributions of pressure and wall shear stress in the rims from two cases.

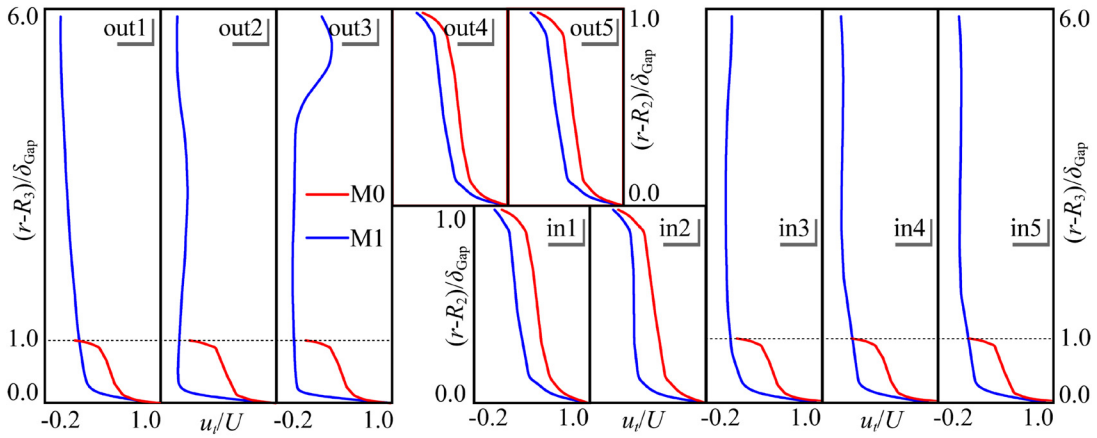


FIG. 17. The dimensionless tangential velocity at different locations in the gap.

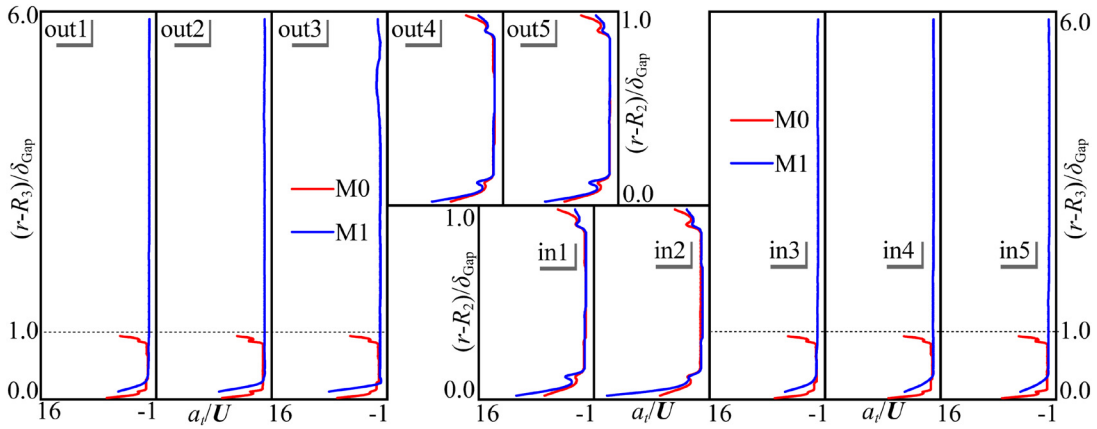


FIG. 18. The radial gradient of the dimensionless tangential velocity in the gap.

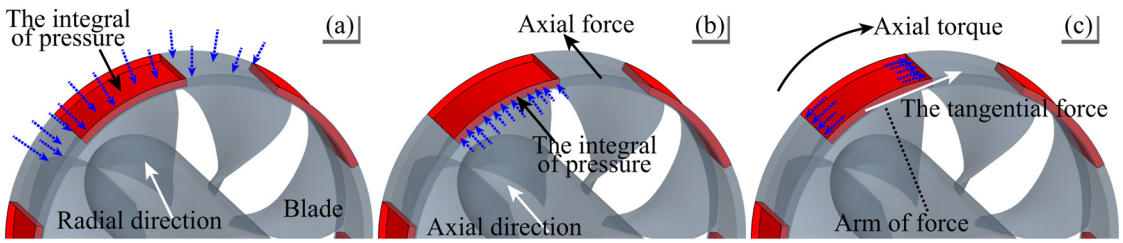


FIG. 19. The hypothesis for the improved propulsive efficiency.

the rotor or rim. In Subsection III B, we find that the leakage vortices have a negligible effect on the inner surface, consistent with the slight variation in the torque in Table VII. Based on Fig. 19(c), the torque that the rotor must overcome is the product of the tangential force (against the direction of rotation) and its radial arm with respect to the center of rotation. For m1SP974, the maximum thickness of the concave cavity is 5 mm, which means the ratio equals 4.74%. The thickness of the concave cavities is so small relative to the radius of the rotor (<5%) that we can simply consider the arm of force to be constant. Thus, the reduced torque is closely related to the tangential force, as shown in Fig. 19(c).

Tables VIII–X list the integral of the pressure and frictional quantities acting on the various surfaces of the rims in two cases. In general, the pressure components are at least one order of magnitude larger than the frictional components. As is well known, the pressure always presses perpendicularly on the wall, which means that the integrals of

**TABLE VIII.** The integral of pressure on various surfaces of the rims.

| Case No. | $S_1$ | $S_2$ | $S_3$ | $CC_{side1}$ |
|---|---|---|---|---|
| M0 | −0.9885 | −14.50 | −41.22 | ... |
| M1 | −3.941 | −17.64 | −61.53 | −0.3967 |
| Case No. | $CC_{side2}$ | $CC_{front}$ | $CC_{back}$ | $CC_{bottom}$ |
| M0 | ... | ... | ... | ... |
| M1 | 0.1846 | 5.002 | −4.935 | −1.839 |

**TABLE IX.** The integral of the tangential wall shear stress on various surfaces of the rims.

| Case No. | $S_1$ | $S_2$ | $S_3$ | $CC_{side1}$ |
|---|---|---|---|---|
| M0 | 0.5376 | 0.3052 | 3.343 | ... |
| M1 | 0.5964 | 0.8155 | 3.091 | 0.4933 |
| Case No. | $CC_{side2}$ | $CC_{front}$ | $CC_{back}$ | $CC_{bottom}$ |
| M0 | ... | ... | ... | ... |
| M1 | 0.5191 | 0 | 0 | 4.504 |

**TABLE X.** The integral of the axial wall shear stress on various surfaces of the rims.

| Case No. | $S_1$ | $S_2$ | $S_3$ | $CC_{side1}$ |
|---|---|---|---|---|
| M0 | 0 | 0 | −0.6148 | ... |
| M1 | 0 | 0 | −0.2303 | 0 |
| Case No. | $CC_{side2}$ | $CC_{front}$ | $CC_{back}$ | $CC_{bottom}$ |
| M0 | ... | ... | ... | ... |
| M1 | 0 | 0.001 624 | 0.013 44 | 0.1773 |

the pressure over $S_3$ and $CC_{bottom}$ are parallel to the radial direction, while the integrals over $S_1$, $S_2$, $CC_{side1}$, and $CC_{side2}$ are parallel to the axial direction. In both cases, the torque involved does not change, as shown in Figs. 19(a) and 19(b). However, the integrals of pressure over $CC_{front}$ and $CC_{back}$ as shown in Fig. 16 are strictly along the tangential direction and contribute to the torque acting on the rotor. If the integral of pressure over the $CC_{front}$ is greater, the torque acting on the rotor or rim will reduce. Conversely, the torque in question decreases. The data in Table VIII correspond exactly to the former phenomenon. Therefore, the propulsive efficiency increases noticeably.

## IV. CONCLUSION AND FUTURE WORK

In this study, the performance of an RDT whose rim was modified with multiple concave cavities was carefully calculated by solving the RANS equations based on STAR CCM+. Compared with the original thruster, the numerical results and analysis yielded the following conclusions:

(1) The concave cavities on the rims improved the hydrodynamic efficiency of the RDT by reducing the torque acting on the rotor (a combination of blades, rim, and partial hub). The increase in the propulsive efficiency was positively correlated with the parameters of the concave cavities. In our study, the best layout of the concave cavities improved efficiency by a maximum of 3.52% and a minimum of 2.01%.
(2) Similar to most previous studies, the pressure difference between the gap inlet and outlet resulted in the flow direction opposite to that of the mainstream within the duct and freestream. The influences of the leakage vortices were limited by the mainstream near the inner surface and prevented from expanding downstream by the blades.
(3) The difference between the integrals of the pressure over $CC_{front}$ and $CC_{back}$ produces a torque in the rotational direction of the rotor, which offsets some of the driving torque or consumption torque. This improves the propulsive efficiency of the RDT.

Concave cavities were found to reduce the consuming torque acting on the rim, with the reduction in torque or increase in efficiency being linear to the concave cavities parameters. The effects of concave cavities on vibration, noise, and cavitation in the RDT require further investigation. In addition, it is unknown whether the structural strength meets the requirements. The optimization of the concave cavity is important for the next study.

## ACKNOWLEDGMENTS

The authors would like to acknowledge the OceanConnect High-Performance Computing Cluster (OceanConnect HPCC) for providing computer resources. This work was supported by the National Natural Science Foundation of China (Grant No. 51579052) and the Key Laboratory Fund for Equipment Pre-research (Grant No. 6142223180210).

## AUTHOR DECLARATIONS

### Conflict of Interest

The authors declare no competing or financial interest.

### Author Contributions

All authors contributed to the conception and design. Mesh division and numerical simulation, data collection and analysis were performed by Peng Li. The first draft of the manuscript was written by Peng Li and all authors commented on previous versions of the manuscript. Chao Wang revised it critically for important intellectual content. Hua-Dong Yao and Kaiqiang Weng helped to perform the analysis with constructive discussions. All authors read and approved the final manuscript.

**Peng Li:** Conceptualization (lead); Investigation (lead); Software (equal); Visualization (equal); Writing – original draft (lead); Writing – review & editing (equal). **Hua-Dong Yao:** Formal analysis (equal); Supervision (equal); Visualization (equal). **Chao Wang:** Supervision (lead); Writing – review & editing (equal). **Kaiqiang Weng:** Methodology (equal); Software (equal).

## DATA AVAILABILITY

The data that support the findings of this study are available from the corresponding author upon reasonable request.

## REFERENCES


[1]K. Song and Y. Kang, "A numerical performance analysis of a rim-driven turbine in real flow conditions," J. Mar. Sci. Eng. **10**(9), 1185 (2022).
[2]H. Bai, B. Yu, W. Ouyang, X. Yan, and J. Zhu, "HF-based sensorless control of a FTPMM in ship shaftless rim-driven thruster system," IEEE Trans. Intell. Transp. Syst. **23**(9), 16867–16877 (2022).
[3]R. R. Tashbulatov, N. A. Atroscshenko, and N. A. Lisovskiy, "Application of combined vane pumps-electric motors with rim transmission of the torque to the impeller," Liq. Gaseous Energy Resour. **1**(2), 108–113 (2021).
[4]J. Lin, H.-D. Yao, C. Wang, Y. Su, and C. Yang, "Hydrodynamic performance of a rim-driven thruster improved with gap geometry adjustment," Eng. Appl. Comput. Fluid Mech. **17**(1), 2183902 (2023).
[5]G. Zhu, R. Li, D. Liao, W. Yang, and P. Zhong, "Lubrication structure design of water lubricated rubber thrust bearing with spiral groove for shaftless rim driven thruster," Tribol. Int. **178**(Part B), 108098 (2023).
[6]B. Liu and M. Vanierschot, "Numerical study of the hydrodynamic characteristics comparison between a ducted propeller and a rim-driven thruster," Appl. Sci. **11**, 4919 (2021).
[7]A. J. Dubas, N. W. Bressloff, H. Fangohr, and S. M. Sharkh, in *Proceedings of the Open Source CFD International Conference 2011* (Open Source CFD, Paris, France, 2011), p. 9.
[8]H. Grümmer, S. Harries, and A. C. Hochbaum, in *Proceedings of the 5th International Symposium on Marine Propulsors Smp'17*, Espoo, Finland (VTT Technical Research Center of Finland Ltd., 2017), pp. 1–9.
[9]S. Kadia, N. Rüther, I. Albayrak, and E. Pummer, "Reynolds stress modeling of supercritical narrow channel flows using OpenFOAM: Secondary currents and turbulent flow characteristics," Phys. Fluids **34**, 125116 (2022).
[10]I. Marusic and J. P. Monty, "Attached eddy model of wall turbulence," Annu. Rev. Fluid Mech. **51**, 49–74 (2019).
[11]J. Gong, J. M. Ding, and L. Z. Wang, "Propeller–duct interaction on the wake dynamics of a ducted propeller," Phys. Fluids **33**(7), 174102 (2021).
[12]S. Zhai, S. Jin, J. Chen, Z. Liu, and X. Song, "CFD-based multi-objective optimization of the duct for a rim-driven thruster," Ocean Eng. **264**, 112467 (2022).
[13]B. W. Song, Y. J. Wang, and W. L. Tian, "Open water performance comparison between hub-type and hubless rim driven thrusters based on CFD method," Ocean Eng. **103**, 55–63 (2015).
[14]Z. Zhu and H. Liu, "The external characteristics and inner flow research of rim-driven thruster," Adv. Mech. Eng. **14**(2), 16878132221081608 (2022).
[15]X. Lü, Q. Zhou, and B. Fang, "Hydrodynamic performance of distributed pump-jet propulsion system for underwater vehicle," J. Hydrodyn. **26**(4), 523–530 (2014).
[16]W. Jiang, X. Liu, L. Liu, and T. Bian, "Numerical analysis of the effect of the blade number on the hydrodynamic performance of shaftless rim-driven thruster," J. Eng. Marit. Eng. **237**(3), 588–596 (2023).
[17]S. Gaggero, "Numerical design of a RIM-driven thruster using a RANS-based optimization approach," Appl. Ocean Res. **94**, 101941 (2020).
[18]Y. Nie, W. Ouyang, Z. Zhang, G. Li, and R. Zheng, "Multi-parameter optimization analysis of hydrodynamic performance for rim-driven thruster," Energies **16**(2), 891 (2023).
[19]S. Sezen, A. Dogrul, C. Delen, and S. Bal, "Investigation of self-propulsion of DARPA suboff by RANS method," Ocean Eng. **150**, 258–271 (2018).
[20]J. Hu, Q. Yan, J. Ding, and S. Sun, "Numerical study on transient four-quadrant hydrodynamic performance of cycloidal propellers," Eng. Appl. Comput. Fluid Mech. **16**(1), 1813–1832 (2022).
[21]K. Song, C. Guo, C. Sun, C. Wang, J. Gong, P. Li, and L. Wang, "Simulation strategy of the full-scale ship resistance and propulsion performance," Eng. Appl. Comput. Fluid Mech. **15**(1), 1321–1342 (2021).
[22]W. Zhang, C. Chen, Z. Wang, Y. Li, H. Guo, J. Hu, H. Li, and C. Guo, "Numerical simulation of structural response during propeller-rudder interaction," Eng. Appl. Comput. Fluid Mech. **15**(1), 584–612 (2021).
[23]Siemens, "Star CCM+ User's Guide,16.06.," 2021.
[24]L. Z. Wang, W. Luo, and M. Li, "Numerical investigation of a propeller operating under different inflow conditions," Phys. Fluids **34**, 105118 (2022).
[25]A. Posa, M. Felli, and R. Broglia, "Influence of an upstream hydrofoil on the acoustic signature of a propeller," Phys. Fluids **34**, 045112 (2022).
[26]L. F. Richardson, "IX. The approximate arithmetical solution by finite differences of physical problems involving differential equations, with an application to the stresses in a masonary dam," Philos. Trans. R. Soc., A **210**, 307–357 (1911).
[27]L. F. Richardson and J. A. Gaunt, "VIII. The deferred approach to the limit," Philos. Trans. R. Soc., A **226**, 299–361 (1927).
[28]A. A. Beige and A. Mardani, "An investigation on flame structure and NOx formation in a gas turbine model combustor using large eddy simulation," Phys. Fluids **35**, 075133 (2023).
[29]C. Guo, C. Yang, C. Sun, C. Wang, H.-D. Yao, and J. Lin, "Numerical investigation of the scale effects of pump-jet propulsor with a pre-swirl stator," Phys. Fluids **35**, 027115 (2023).
[30]C. Wang, P. Li, Y. Han, and L. Hao, "The study on the wake of a CLT propeller under different advance coefficients," Appl. Ocean Res. **118**, 102996 (2022).
[31]C. Wang, P. Li, C. Guo, L. Wang, and S. Sun, "Numerical research on the instabilities of CLT propeller wake," Ocean Eng. **243**, 110305 (2022).
[32]X. D. Tong, H. Y. Chen, and Y. Chen, "Low frequency broadband noise radiated by highly skewed propeller ingesting inflow turbulence," J. Sound Vib. **490**, 115709 (2021).
[33]I. B. Celik, U. Ghia, P. J. Roache, C. J. Freitas, H. Coleman, and P. E. Raad, "Procedure for estimation and reporting of uncertainty due to discretization in CFD applications," J. Fluids Eng. **130**(7), 078001 (2008).
[34]J. Baltazar, J. A. C. Falcão de Campos, and J. Bosschers, "Open-water thrust and torque predictions of a ducted propeller system with a panel method," Int. J. Rotating Mach. **2012**, 474785.
[35]A. J. Dubas, "Robust automated computational fluid dynamics analysis and design optimisation of rim driven thrusters," Ph.D. thesis (University of Southampton, 2014).
[36]H. Jiang, W. Ouyang, C. Sheng, J. Lan, and R. Bucknall, "Numerical investigation on hydrodynamic performance of a novel shaftless rim-driven counter-rotating thruster considering gap fluid," Appl. Ocean Res. **118**, 102967 (2022).
[37]K. Croci, F. Ravelet, A. Danlos, J.-C. Robinet, and L. Barast, "Attached cavitation in laminar separations within a transition to unsteadiness," Phys. Fluids **31**, 1 (2019).